Section S7. The BSLE from different containers

The main experimental results were obtained by hosting the nanoparticles in a cylindrical glass container (Fig. S7). To show that the curved surface has negligible influence to our observed results, we also performed some experiments using cubic containers to host the samples, as shown in Fig. S7. The experimental setup is the same as it in Fig. 1a, and the incident light is *x*-polarized. The experimental results in Fig. S7 show that the shape of container will not change the observation of our BSLE.

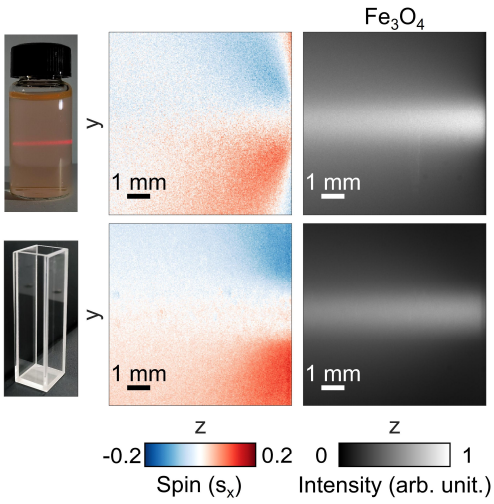

Fig.S7 Experiments with different sample containers.

Section S8. Scattering theory

In this section, we present detailed theory derivations of the near-field and far-field characteristics of the linearly-polarized plane wave scattered from spherical nanoparticles (Mie theory). Note that in our experiments, the distance between nanoparticles is much larger than the wavelength, so the overall second scattering is dominated by far-field features. Here, we particularly focus on the spin angular momentum distribution and spin-momentum locking relations for different Mie scattering. Several typical resonant modes are shown as examples. We will see the scattering system (3D electromagnetic field) has different spin properties from those of 2D evanescent waves. This spin property also changes drastically between different harmonic modes or from their combinations. Therefore, multiple scattering provides a complicated environment for observing spin optical effects. In the following, we assume the incident light is an *x*-polarized plane wave propagating along the *z*-axis.

A. Spin-orbit relation of light for typical multipole scattering

Mie scattering describes the scattered field of a plane wave by a spherical particle (*3*). The solution to Maxwell's equations can be expressed as a superposition of vector spherical harmonics (*3*), which corresponds to the multipole expansion of electromagnetic field. The scattered electric and magnetic fields are

$$\mathbf{E} = \sum_{n=1}^{\infty} E_n\left(\mathrm{i}a_n\mathbf{N}_{e1n}^{(3)} - b_n\mathbf{M}_{o1n}^{(3)}\right),$$
$$\mathbf{H} = \frac{k}{\omega\mu}\sum_{n=1}^{\infty} E_n\left(\mathrm{i}b_n\mathbf{N}_{o1n}^{(3)} + a_n\mathbf{M}_{e1n}^{(3)}\right). \qquad \textbf{(S1)}$$

Here, $E_n = \frac{\mathrm{i}^n E_0(2n+1)}{n(n+1)}$, $n \in \mathbf{Z}$. E_0 is the electric amplitude of the incident light. $k = \sqrt{\varepsilon\mu}\omega$ is the wave vector outside the particle, where ω is the angular frequency, and ε and μ represent the dielectric permittivity and magnetic permeability of the environment, respectively. The Mie coefficients a_n, b_n represent the complex amplitudes of the electric and magnetic harmonics, respectively. They are determined by the incident wavelength, and by the size and refractive index of the particle. The $\mathbf{N}_{e,o1n}^{(3)}$ and $\mathbf{M}_{e,o1n}^{(3)}$ are the electric and magnetic vector spherical harmonics, respectively. The superscript (3) means that the radial part of the generating functions is spherical Hankel functions of the first kind (*3*). Conventionally, we discuss Mie scattering in spherical coordinates (r, θ, ϕ), where r is the radial distance from the particle center, θ is the polar angle and ϕ is the azimuthal angle. In the following subsections, we present several typical spin-orbit interactions of scattering from individual nanoparticles as derived from Mie theory, Eq. (**S1**).

A1. Electric dipole

The simplest case of Mie scattering is an electric dipole approximation, also known as Rayleigh scattering. This happens when the size of a particle is very small compared to the incident wavelength. In this case, only a_1 is non-zero. The electric field $\mathbf{E}$, magnetic field $\mathbf{H}$, spin angular momentum (SAM) density $\mathbf{s} = \mathrm{Im}\left[\frac{\varepsilon}{4\omega}\mathbf{E}^* \times \mathbf{E} + \frac{\mu}{4\omega}\mathbf{H}^* \times \mathbf{H}\right]$, and the kinetic momentum density $\mathbf{p} = \frac{\varepsilon\mu}{2}\mathrm{Re}[\mathbf{E} \times \mathbf{H}^*]$ can be derived from Eq. (**S1**), with the results summarized below,

$$\mathbf{E}_{a_1} = -E_1 a_1 e^{\mathrm{i}kr}\left[\left(-\frac{2\mathrm{i}}{k^2r^2} + \frac{2}{k^3r^3}\right)\cos\phi\sin\theta\,\hat{\boldsymbol{e}}_{\boldsymbol{r}} - \left(-\frac{1}{kr} - \frac{\mathrm{i}}{k^2r^2} + \frac{1}{k^3r^3}\right)\cos\phi\cos\theta\,\hat{\boldsymbol{e}}_{\boldsymbol{\theta}} + \left(-\frac{1}{kr} - \frac{\mathrm{i}}{k^2r^2} + \frac{1}{k^3r^3}\right)\sin\phi\,\hat{\boldsymbol{e}}_{\boldsymbol{\phi}}\right],$$
$$\mathbf{H}_{a_1} = -\frac{k}{\omega\mu}E_1 a_1 e^{\mathrm{i}kr}\left[\left(\frac{1}{kr} + \frac{\mathrm{i}}{k^2r^2}\right)\sin\phi\,\hat{\boldsymbol{e}}_{\boldsymbol{\theta}} + \left(\frac{1}{kr} + \frac{\mathrm{i}}{k^2r^2}\right)\cos\phi\cos\theta\,\hat{\boldsymbol{e}}_{\boldsymbol{\phi}}\right],$$

$$\mathbf{s}_{a_1} = \frac{\varepsilon}{2k\omega}|E_1|^2|a_1|^2\left[\frac{\sin 2\phi \sin\theta}{k^2r^3}\hat{\boldsymbol{e}}_{\boldsymbol{\theta}} + \frac{\cos^2\phi \sin 2\theta}{k^2r^3}\hat{\boldsymbol{e}}_{\boldsymbol{\phi}}\right],$$

$$\mathbf{p}_{a_1} = \frac{\varepsilon k}{2\omega}|E_1|^2|a_1|^2\left[\frac{1}{k^2r^2}(\cos^2\phi\cos^2\theta + \sin^2\phi)\hat{\boldsymbol{e}}_{\boldsymbol{r}}\right].$$

For an electric dipole, the SAM density of the scattered field originates only from the electric field. This SAM density decays in space following a $1/r^3$ rule, hence it exists in the nearfield and dissipates away from the source. However, this $1/r^3$ decaying rule is still very different from the transverse spin of surface plasmon polaritons (or generally, surface evanescent waves), which decay exponentially. Particularly, we will find here the SAM density is locked to the kinetic momentum density with a unique relation:

$$\nabla \times \mathbf{p} = k^2\mathbf{s}. \qquad \textbf{(S2)}$$

One will notice a general relation in reference (*5*), $\mathbf{s} = \frac{1}{2k^2}\nabla \times \mathbf{p} + \frac{\varepsilon\mu}{4k^2}\mathrm{Re}[\mathbf{E}^* \cdot (\boldsymbol{\nabla})\mathbf{H} - \mathbf{H}^* \cdot (\boldsymbol{\nabla})\mathbf{E}]$, where the first term is named "Poynting spin" and the last term is named "canonical spin". In structured surface waves (*4*) and evanescent waves, the canonical spin is zero, resulting in $\nabla \times \mathbf{p} = 2k^2\mathbf{s}$, while in a linearly polarized dipole, the canonical spin equals to the Poynting spin, resulting in $\nabla \times \mathbf{p} = k^2\mathbf{s}$. This spin-momentum locking relation in Eq. (**S2**) is a unique property of dipole emitter in three-dimensional space. Previously, the study of spin-orbit interaction in scattering considered the dipole contribution, but without including the evanescent field (*6*).

A2. Magnetic dipole

Magnetic dipole corresponds to the Mie coefficient b_1. While the incident light is *x*-polarized and propagates along the *z*-axis, the excited magnetic dipole is *y*-polarized. The electric field $\mathbf{E}$, magnetic field $\mathbf{H}$, SAM density $\mathbf{s}$, and the kinetic momentum density $\mathbf{p}$ of the scattered field are expressed below,

$$\mathbf{E}_{b_1} = -E_1 b_1 e^{\mathrm{i}kr}\left[\left(\frac{1}{kr} + \frac{\mathrm{i}}{k^2r^2}\right)\cos\phi\,\hat{\boldsymbol{e}}_{\boldsymbol{\theta}} - \left(\frac{1}{kr} + \frac{\mathrm{i}}{k^2r^2}\right)\sin\phi\cos\theta\,\hat{\boldsymbol{e}}_{\boldsymbol{\phi}}\right],$$

$$\mathbf{H}_{b_1} = -\frac{k}{\omega\mu}E_1 b_1 e^{\mathrm{i}kr}\left[\left(-\frac{2\mathrm{i}}{k^2r^2} + \frac{2}{k^3r^3}\right)\sin\phi\sin\theta\,\hat{\boldsymbol{e}}_{\boldsymbol{r}} - \left(-\frac{1}{kr} - \frac{\mathrm{i}}{k^2r^2} + \frac{1}{k^3r^3}\right)\sin\phi\cos\theta\,\hat{\boldsymbol{e}}_{\boldsymbol{\theta}} - \left(-\frac{1}{kr} - \frac{\mathrm{i}}{k^2r^2} + \frac{1}{k^3r^3}\right)\cos\phi\,\hat{\boldsymbol{e}}_{\boldsymbol{\phi}}\right],$$

$$\mathbf{s}_{b_1} = \frac{\varepsilon}{2k\omega}|E_1|^2|b_1|^2\left[-\frac{\sin 2\phi \sin\theta}{k^2r^3}\hat{\boldsymbol{e}}_{\boldsymbol{\theta}} + \frac{\sin^2\phi \sin 2\theta}{k^2r^3}\hat{\boldsymbol{e}}_{\boldsymbol{\phi}}\right],$$

$$\mathbf{p}_{b_1} = \frac{\varepsilon k}{2\omega}|E_1|^2|b_1|^2\left[\frac{1}{k^2r^2}(\cos^2\theta\sin^2\phi + \cos^2\phi)\hat{\boldsymbol{e}}_{\boldsymbol{r}}\right].$$

The results are similar to those obtained from the electric dipole because of the electric-magnetic symmetry. For the magnetic dipole, the SAM density of the scattered field originates only from the magnetic field. Similarly, the SAM density is perpendicular to the kinetic momentum density and they satisfy the same spin-momentum locking relation described by Eq. (**S2**).

A3. Electric quadrupole

The electric quadrupole corresponds to Mie coefficient a_2. The electric field **E**, magnetic field **H**, SAM density **s** and the kinetic momentum density **p** of scattered field are expressed as

$$\mathbf{E}_{a_2} = E_2 a_2 e^{\mathrm{i}kr}\left[-9\left(-\frac{1}{k^2r^2}-\frac{3\mathrm{i}}{k^3r^3}+\frac{3}{k^4r^4}\right)\cos\phi\sin 2\theta\,\hat{\boldsymbol{e}}_{\boldsymbol{r}} - 3\left(-\frac{\mathrm{i}}{kr}+\frac{3}{k^2r^2}+\frac{6\mathrm{i}}{k^3r^3}-\frac{6}{k^4r^4}\right)\cos\phi\cos 2\theta\,\hat{\boldsymbol{e}}_{\boldsymbol{\theta}} + 3\left(-\frac{\mathrm{i}}{kr}+\frac{3}{k^2r^2}+\frac{6\mathrm{i}}{k^3r^3}-\frac{6}{k^4r^4}\right)\sin\phi\cos\theta\,\hat{\boldsymbol{e}}_{\boldsymbol{\phi}}\right],$$

$$\mathbf{H}_{a_2} = \frac{k}{\omega\mu}E_2 a_2 e^{\mathrm{i}kr}\left[3\left(\frac{\mathrm{i}}{kr}-\frac{3}{k^2r^2}-\frac{3\mathrm{i}}{k^3r^3}\right)\sin\phi\cos\theta\,\hat{\boldsymbol{e}}_{\boldsymbol{\theta}} + 3\left(\frac{\mathrm{i}}{kr}-\frac{3}{k^2r^2}-\frac{3\mathrm{i}}{k^3r^3}\right)\cos\phi\cos 2\theta\,\hat{\boldsymbol{e}}_{\boldsymbol{\phi}}\right],$$

$$\mathbf{s}_{a_2} = \frac{\varepsilon}{2k\omega}|E_2|^2|a_2|^2\left[\frac{27\sin 2\phi\sin 2\theta\cos\theta}{2k^2r^3}\hat{\boldsymbol{e}}_{\boldsymbol{\theta}} + \frac{27\cos^2\phi\sin 4\theta}{2k^2r^3}\hat{\boldsymbol{e}}_{\boldsymbol{\phi}}\right],$$

$$\mathbf{p}_{a_2} = \frac{\varepsilon k}{2\omega}|E_2|^2|b_2|^2\left[\frac{9}{k^2r^2}(\cos^2 2\theta\cos^2\phi + \cos^2\theta\sin^2\phi)\hat{\boldsymbol{e}}_{\boldsymbol{r}}\right].$$

In this case, the SAM density is still perpendicular to the kinetic momentum density. However, they are not constrained by the spin-momentum locking relation of Eq. (**S2**).

A4. Magnetic quadrupole

The magnetic quadrupole is from the Mie coefficient b_2. The electric field **E**, magnetic field **H**, SAM density **s** and the kinetic momentum density **p** of scattered field are expressed as below,

$$\mathbf{E}_{b_2} = E_2 b_2 e^{\mathrm{i}kr}\left[3\left(\frac{\mathrm{i}}{kr}-\frac{3}{k^2r^2}-\frac{3\mathrm{i}}{k^3r^3}\right)\cos\phi\cos\theta\,\hat{\boldsymbol{e}}_{\boldsymbol{\theta}} - 3\left(\frac{\mathrm{i}}{kr}-\frac{3}{k^2r^2}-\frac{3\mathrm{i}}{k^3r^3}\right)\sin\phi\cos 2\theta\,\hat{\boldsymbol{e}}_{\boldsymbol{\phi}}\right],$$

$$\mathbf{H}_{b_2} = \frac{k}{\omega\mu}E_2 b_2 e^{\mathrm{i}kr}\left[-9\left(-\frac{1}{k^2r^2}-\frac{3\mathrm{i}}{k^3r^3}+\frac{3}{k^4r^4}\right)\sin\phi\sin 2\theta\,\hat{\boldsymbol{e}}_{\boldsymbol{r}} - 3\left(-\frac{\mathrm{i}}{kr}+\frac{3}{k^2r^2}+\frac{6\mathrm{i}}{k^3r^3}-\frac{6}{k^4r^4}\right)\sin\phi\cos 2\theta\,\hat{\boldsymbol{e}}_{\boldsymbol{\theta}} - 3\left(-\frac{\mathrm{i}}{kr}+\frac{3}{k^2r^2}+\frac{6\mathrm{i}}{k^3r^3}-\frac{6}{k^4r^4}\right)\cos\phi\cos\theta\,\hat{\boldsymbol{e}}_{\boldsymbol{\phi}}\right],$$

$$\mathbf{s}_{b_2} = \frac{\varepsilon}{2k\omega}|E_2|^2|b_2|^2\left[-\frac{27\sin 2\phi \sin 2\theta\cos\theta}{2k^2r^3}\hat{\boldsymbol{e}}_{\boldsymbol{\theta}} + \frac{27\sin^2\phi\sin 4\theta}{2k^2r^3}\hat{\boldsymbol{e}}_{\boldsymbol{\phi}}\right],$$

$$\mathbf{p}_{b_2} = \frac{\varepsilon k}{2\omega}|E_2|^2|b_2|^2\left[\frac{9}{k^2r^2}(\cos^2 2\theta\sin^2\phi + \cos^2\theta\cos^2\phi)\hat{\boldsymbol{e}}_{\boldsymbol{r}}\right].$$

Akin to the electric quadrupole, the SAM density here is always perpendicular to the kinetic momentum density. However, they are not quantitatively constrained by the spin-momentum locking relation of Eq. (**S2**).

A5. Huygens dipole

While a single mode analysis is theoretically interesting for the understanding of the basic spin properties of scattering, the interaction between different modes is more common for natural particles. Here, we consider multipole response of the particle with Mie coefficient $a_1 = b_1$. This emitter is known as a Huygens dipole (*7*), which meets a Kerker condition (*8*). The SAM density $\mathbf{s}$ and the kinetic momentum density $\mathbf{p}$ of scattered field are expressed as below,

$$\mathbf{s} = \mathbf{s}_{a_1} + \mathbf{s}_{b_1} + \mathbf{s}_{coupling}$$

$$\mathbf{s}_{a_1} + \mathbf{s}_{b_1} = \frac{\varepsilon}{2k\omega}|E_1|^2|a_1|^2\frac{\sin 2\theta}{k^2r^3}\hat{\boldsymbol{e}}_{\boldsymbol{\phi}},$$

$$\mathbf{s}_{coupling} = \frac{\varepsilon}{2k\omega}|E_1|^2|a_1|^2\left(\frac{2\sin\theta}{k^2r^3} + \frac{2\sin\theta}{k^4r^5}\right)\hat{\boldsymbol{e}}_{\boldsymbol{\varphi}},$$

$$\mathbf{s} = \frac{\varepsilon}{2k\omega}E_0^2|a_1|^2\left[\frac{9}{4}\left(\frac{2\sin\theta(1+\cos\theta)}{k^2r^3} + \frac{2\sin\theta}{k^4r^5}\right)\hat{\boldsymbol{e}}_{\boldsymbol{\phi}}\right],$$

$$\mathbf{p} = \mathbf{p}_{a_1} + \mathbf{p}_{b_1} + \mathbf{p}_{coupling}$$

$$\mathbf{p}_{a_1} + \mathbf{p}_{b_1} = \frac{\varepsilon k}{2\omega}|E_1|^2|a_1|^2\frac{(\cos^2\theta+1)}{k^2r^2}\hat{\boldsymbol{e}}_{\boldsymbol{r}},$$

$$\mathbf{p}_{coupling} = \frac{\varepsilon k}{2\omega}|E_1|^2|a_1|^2\left[\left(\frac{2\cos\theta}{k^2r^2} + \frac{\cos\theta}{k^6r^6}\right)\hat{\boldsymbol{e}}_{\boldsymbol{r}} + \frac{2\sin\theta}{k^6r^6}\hat{\boldsymbol{e}}_{\boldsymbol{\theta}}\right],$$

$$\mathbf{p} = \frac{\varepsilon k}{2\omega}E_0^2|a_1|^2\frac{9}{4}\left\{\left[\frac{1}{k^2r^2}(1+\cos\theta)^2 + \frac{1}{k^6r^6}\cos\theta\right]\hat{\boldsymbol{e}}_{\boldsymbol{r}} + \frac{2\sin\theta}{k^6r^6}\hat{\boldsymbol{e}}_{\boldsymbol{\theta}}\right\}.$$

The SAM and momentum are a mixture of individual contributions from the electric dipole, magnetic dipole, and their interference (coupling). Through the entire space, the individual contributions of a_1 and b_1 satisfy the spin-momentum locking relation: $\nabla\times\left(\mathbf{p}_{a_1} + \mathbf{p}_{b_1}\right) = k^2\left(\mathbf{s}_{a_1} + \mathbf{s}_{b_1}\right)$. For a spatial region with negligible

$1/r^5$ and $1/r^6$, we have $\nabla \times \mathbf{p}_{coupling} = k^2 \mathbf{s}_{coupling}$. Therefore, the spin-momentum locking relation Eq. **(S2)** also works for Huygens dipole, as long as we can ignore the $1/r^5$ and $1/r^6$ terms.

A6. Janus dipole

Aside from the Huygens dipole, there is another very interesting scattering known as Janus dipole, which is defined by $b_1 = \mathrm{i}a_1$. The Janus dipole has been studied for unidirectional spin coupling and unusual nearfield spin/momentum properties (*9-13*). Here, we give the exact SAM density $\mathbf{s}$, and the kinetic momentum density $\mathbf{p}$ of the Janus dipole,

$$\mathbf{s} = \mathbf{s}_{a_1} + \mathbf{s}_{b_1} + \mathbf{s}_{coupling}$$

$$\mathbf{s}_{a_1} + \mathbf{s}_{b_1} = \frac{\varepsilon}{2k\omega}|E_1|^2|a_1|^2 \frac{\sin 2\theta}{k^2 r^3}\hat{\boldsymbol{e}}_{\boldsymbol{\phi}},$$

$$\mathbf{s}_{coupling} = \frac{\varepsilon}{2k\omega}|E_1|^2|a_1|^2 \frac{\sin^2\theta \sin 2\phi}{kr^2}\hat{\boldsymbol{e}}_{\boldsymbol{r}},$$

$$\mathbf{s} = \frac{\varepsilon}{2k\omega}E_0^2|a_1|^2\left[\frac{9}{4}\left(\frac{\sin^2\theta \sin 2\phi}{kr^2}\hat{\boldsymbol{e}}_{\boldsymbol{r}} + \frac{\sin 2\theta}{k^2 r^3}\hat{\boldsymbol{e}}_{\boldsymbol{\phi}}\right)\right],$$

$$\mathbf{p}_{a_1} + \mathbf{p}_{b_1} = \frac{\varepsilon k}{2\omega}|E_1|^2|a_1|^2 \frac{(\cos^2\theta+1)}{k^2 r^2}\hat{\boldsymbol{e}}_{\boldsymbol{r}},$$

$$\mathbf{p}_{coupling} = \frac{\varepsilon k}{2\omega}|E_1|^2|a_1|^2\left[\frac{2\cos 2\phi \sin\theta}{k^2 r^2}\hat{\boldsymbol{e}}_{\boldsymbol{\theta}} - \frac{\sin 2\phi \sin 2\theta}{k^3 r^3}\hat{\boldsymbol{e}}_{\boldsymbol{\phi}}\right],$$

$$\mathbf{p} = \frac{\varepsilon k}{2\omega}E_0^2|a_1|^2\left[\frac{9}{4}\left(\frac{1+\cos^2\theta}{k^2 r^2}\hat{\boldsymbol{e}}_{\boldsymbol{r}} + \frac{2\cos 2\phi \sin\theta}{k^3 r^3}\hat{\boldsymbol{e}}_{\boldsymbol{\theta}} - \frac{\sin 2\phi \sin 2\theta}{k^3 r^3}\hat{\boldsymbol{e}}_{\boldsymbol{\phi}}\right)\right].$$

We can see that the SAM of a Janus dipole is a far field effect ($\mathbf{s}$~$1/r^2$), which means it can be detected even if $r >> \lambda$. The uncoupled terms of SAM density and the kinetic momentum density satisfy the spin-orbit relation: $\nabla \times (\mathbf{p}_{a_1} + \mathbf{p}_{b_1}) = k^2(\mathbf{s}_{a_1} + \mathbf{s}_{b_1})$. Additionally, SAM is in parallel or antiparallel to the kinetic momentum in the far field, depending on the sign of the spatial coordinate ϕ. Therefore, we have

$$\mathbf{s} = \frac{9\varepsilon}{8k\omega}E_0^2|a_1|^2\left(\frac{\sin^2\theta}{kr^2}\hat{\boldsymbol{e}}_{\boldsymbol{r}}\right)\sin 2\phi. \qquad \textbf{(S3)}$$

From Eq. (**S3**), we can predict a momentum-space spin Hall effect of light from a Janus dipole scattering, while the spin depends on the observation angle of ϕ.

B. Spin distribution of scattering field of multipoles

We particularly studied the spin contributions from combined a_1, b_1, and combined a_1, a_2, as they are significantly larger than the other Mie coefficients for the nanoparticles used in our experiment. The *x*-polarized incident light propagates along the *z*-direction and is scattered by a spherical nanoparticle, as shown in Fig. S8a. The SAM density obtained at the location (marked as a black dot in Fig. S8a, 10λ away from the scatter) changes with the phase and amplitude differences of a_1, b_1 and a_1, a_2, resulting in a spin-locking effect phase diagram shown in Fig. S8b. Notably, the SAM is strong if there is a $\pm\pi/2$ phase difference between the two coupled modes, and disappears if the phase difference approaches 0 or π. Therefore, the spin-locking effect is generalized from Janus dipole (Eq. S3) to other combinations of two modes with a phase difference. The highlighted points in Fig. S8b are typical combinations of two given modes with different phases and amplitudes. Their spin textures around the scatterer ($r = 10\lambda$) are represented in Fig. S8c, where we sketched a light radiation cone for every case. These scattering cases are divided into three different types. One, for instance, the electric dipole, represents topological-insulator-like spin textures with two orbital spin distributions perpendicular to the radiation cones (a_1, b_1, a_2 = 1, 0, 0). This is a typical transverse spin. For the Janus dipole, the spins are parallel to the radiation cones (a_1, b_1, a_2 = 1, i, 0), that is, longitudinal spin. In general, the spin from scattering is neither perpendicular nor parallel to the kinetic momentum. This property can be studied by calculating the spin as a function of propagating distance away from the particle. As shown in Fig. S9a, for electric dipole, electric quadrupole and Huygens dipole, the SAM of scattered field is always perpendicular to $\hat{\boldsymbol{e}}_{\boldsymbol{r}}$. For Janus dipole, the SAM is approximately perpendicular to $\hat{\boldsymbol{e}}_{\boldsymbol{r}}$ in the near field, and as the radial distance increases, the SAM tends to be gradually aligned with $\hat{\boldsymbol{e}}_{\boldsymbol{r}}$. This is because for the Janus dipole, $\mathbf{s} \propto \frac{\sin^2\theta \sin 2\phi}{kr^2}\hat{\boldsymbol{e}}_{\boldsymbol{r}} + \frac{\sin 2\theta}{k^2 r^3}\hat{\boldsymbol{e}}_{\boldsymbol{\phi}}$. Additionally, we investigate the variation of radial component of SAM with respect to the radial distance, as shown in Fig. S9b. When the coupling phase between different multipoles is 0, the radial component of the SAM rapidly decays and vanishes in the far field. However, when the coupling phase is $\pi/2$, it can propagate to the far field with a constant spin.

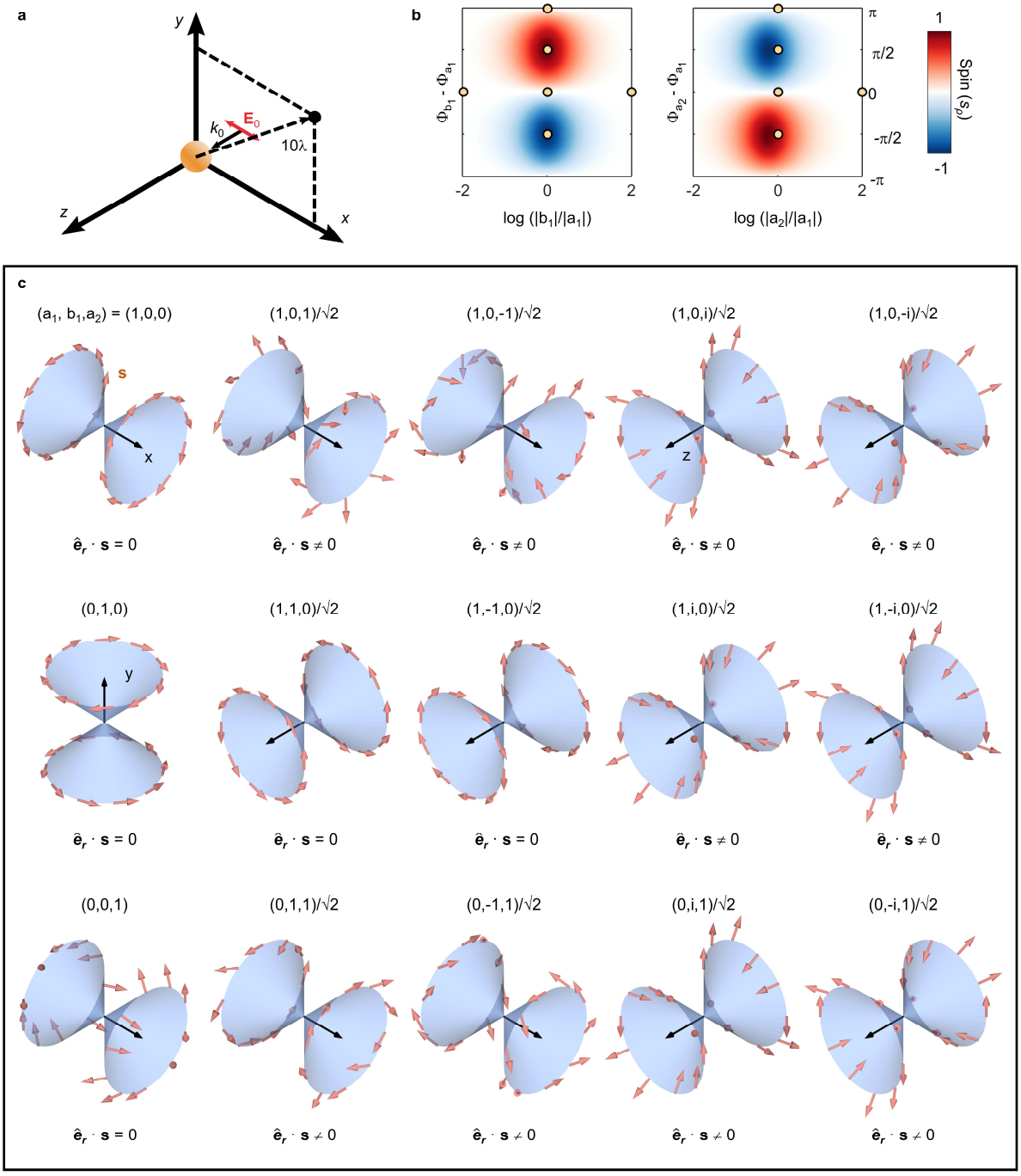

Fig. S8 SAM properties of the scattering field for different combinations of multipoles. (a) Schematic of Mie scattering. The location of the black dot in the figure is $(5\sqrt{2}\lambda, 5\sqrt{2}\lambda, 0)$ **(b)** Phase diagram of s_ρ at the black dot in (a) with respect to Mie scattering coefficients. s_ρ represents the radial component of SAM density in the *xy* plane. $\Phi_{a_1}, \Phi_{b_1}, \Phi_{a_2}$ represent the phases of a_1, b_1, a_2, respectively. **(c)** SAM distributions of the Mie scattering field under different combinations of Mie coefficients. The orange arrows represent the SAM.

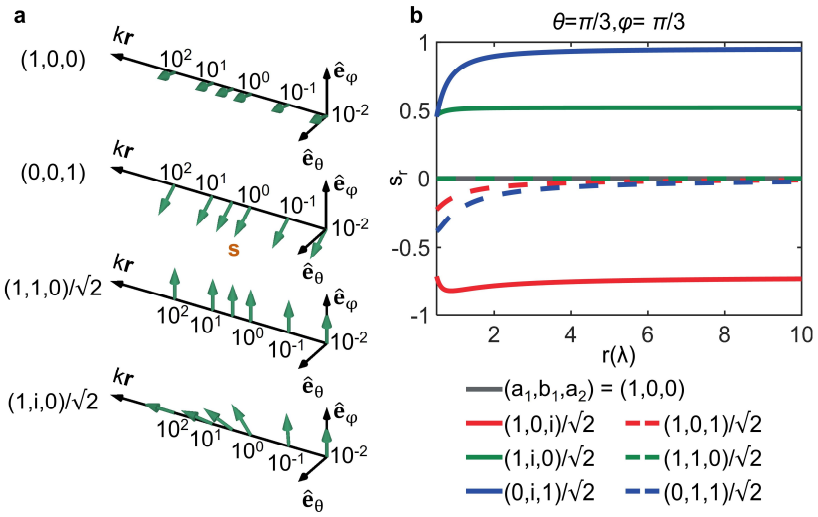

Fig.S9 The SAM density of scattering field as a function of propagation distance. (a) The change of SAM's direction with respect to kr along the direction of $\theta = \pi/3$, $\varphi = \pi/3$. The green arrows represent the direction of the SAM. **(b)** The normalized radial component of SAM as a function of r, which is calculated along the direction of $\theta = \pi/3, \varphi = \pi/3$. $\mathbf{s}_{nor} = \mathrm{Im}[\varepsilon\mathbf{E}^* \times \mathbf{E} + \mu\mathbf{H}^* \times \mathbf{H}]/(\varepsilon|\mathbf{E}|^2 + \mu|\mathbf{H}|^2)$, $s_r = \mathbf{s}_{nor} \cdot \hat{\boldsymbol{e}}_r$.

C. SAM density in the far field – the universality of spin effects

From previous theory, we have understood that the Janus dipole, and the electric dipole and quadrupolar combinations, can give rise to far field spin effect akin to a spin Hall effect. Here, we give a theoretical derivation to show the general conditions one requires to obtain far field spin effect from the Mie scattering, which is excited by a linearly polarized incident laser. Considering kr>>1, the scattering electric fields are given as (*3*)

$$E_\theta \sim E_0 \frac{e^{i\rho}}{-i\rho} \cos\phi \, S_2(\cos\theta), \text{ and}$$

$$E_\phi \sim -E_0 \frac{e^{i\rho}}{-i\rho} \sin\phi \, S_1(\cos\theta),$$

where $S_1 = \sum_n \frac{(2n+1)}{n(n+1)}(a_n\pi_n + b_n\tau_n)$, $S_2 = \sum_n \frac{(2n+1)}{n(n+1)}(a_n\tau_n + b_n\pi_n)$ and $\pi_n = \frac{P_n^1(\cos\theta)}{\sin\theta}$, $\tau_n = \frac{dP_n^1(\cos\theta)}{d\theta}$, $\rho = kr$.

The electric component of SAM density is given by

$$\mathbf{s}_{\mathrm{e}} \propto \mathrm{Im}[\mathbf{E}^* \times \mathbf{E}] = \mathrm{Im}[S_1^* S_2 - S_1 S_2^*] E_0^2 \sin\phi \cos\phi \frac{1}{\rho^2} \hat{\boldsymbol{e}}_{\boldsymbol{r}}$$

$$= \sum_{m,n} \frac{(2m+1)}{m(m+1)} \cdot \frac{(2n+1)}{n(n+1)}$$

$$\cdot \begin{bmatrix} -2\pi_m \tau_n |a_m||a_n| \sin(\varphi_{a_m} - \varphi_{a_n}) - 2\pi_n \tau_m |b_m||b_n| \sin(\varphi_{b_m} - \varphi_{b_n}) \\ -2\pi_m \pi_n |a_m||b_n| \sin(\varphi_{a_m} - \varphi_{b_n}) - 2\tau_m \tau_n |a_n||b_m| \sin(\varphi_{b_m} - \varphi_{a_n}) \end{bmatrix} E_0^2 \sin\phi \cos\phi \frac{1}{\rho^2} \hat{\boldsymbol{e}}_{\boldsymbol{r}}$$

(S4)

From Eq. (**S4**), we will see that if there is a non-zero or non-π phase difference between any two different multipole components, the SAM will propagate to the far field as a radial component. Of course, the SAM will propagate to the far field as well if the incident wave is elliptically or circularly polarized. In those cases, the non-zero phase difference between any two different multipole components are generated from the incident polarization, rather than from the nanoparticle's response.

D. The geometric phase from scattering matrix

To theoretically demonstrate that the spin-locking phenomena can be detected from *x*-axis direction in our experiment, we used the far-field scattering matrix to analyze the relationship between the incident electric field and in the Mie scattering of a single particle. It is well-understood that the spin split phenomena of light usually are interpreted by a geometric phase effect. Mostly, this geometric phase effect is achieved by using rotated anisotropic structures (*14*), or curved optical paths (*15*). We will show that in our experiments, the geometric phase naturally arises from the scattered 3D electric field by the nanoparticles. As mentioned before, the scattered far field is

$$\mathbf{E}_{\mathrm{s}} = E_0 \frac{e^{\mathrm{i}\rho}}{-\mathrm{i}\rho} \cos\phi \, S_2 \hat{\boldsymbol{e}}_{\boldsymbol{\theta}} - E_0 \frac{e^{\mathrm{i}\rho}}{-\mathrm{i}\rho} \sin\phi \, S_1 \hat{\boldsymbol{e}}_{\boldsymbol{\phi}} = E_0 \frac{e^{\mathrm{i}\rho}}{-\mathrm{i}\rho} \big[(S_2 \cos\theta \cos^2\phi + S_1 \sin^2\phi) \, \hat{\boldsymbol{e}}_{\boldsymbol{x}} +$$

$$(S_2 \cos\theta \cos\phi \sin\phi - S_1 \cos\phi \sin\phi) \, \hat{\boldsymbol{e}}_{\boldsymbol{y}} - S_2 \sin\theta \cos\phi \, \hat{\boldsymbol{e}}_{\boldsymbol{z}} \big].$$

The scattering field is related to the incident field through a scattering matrix **M**, with

$$\mathbf{E}_{\mathrm{s}} = \mathbf{M} \times \mathbf{E}_0, \text{ and}$$

$$\mathbf{E}_0 = \begin{bmatrix} E_x \\ E_y \\ 0 \end{bmatrix}.$$

Based on this relation, we have $\mathbf{E}_\mathrm{s} = E_0 \frac{e^{\mathrm{i}\rho}}{-\mathrm{i}\rho} \cos\phi\, S_2 \hat{\boldsymbol{e}}_{\boldsymbol{\theta}} - E_0 \frac{e^{\mathrm{i}\rho}}{-\mathrm{i}\rho} \sin\phi\, S_1 \hat{\boldsymbol{e}}_{\boldsymbol{\phi}}$. By using the rotational symmetry condition $\mathbf{E}_\mathrm{s}(\phi; x-\text{polarized}) = \mathbf{E}_\mathrm{s}\left(\phi + \frac{\pi}{2}; y-\text{polarized}\right)$, where *x*- or *y*-polarized denotes the polarization of the incident light, we can derive a specific form of the scattering matrix:

$$\begin{bmatrix} E_{sy} \\ E_{sz} \end{bmatrix} = \frac{e^{\mathrm{i}k(r-z)}}{-\mathrm{i}kr} \begin{bmatrix} \frac{1}{2} S_2 \cos\theta \sin 2\phi - \frac{1}{2} S_1 \sin 2\phi & S_2 \cos\theta \sin^2\phi + S_1 \cos^2\phi \\ -S_2 \sin\theta \cos\phi & -S_2 \sin\theta \sin\phi \end{bmatrix} \begin{bmatrix} E_x \\ E_y \end{bmatrix}. \quad \text{(S5)}$$

Therefore, considering the *xy* plane as the incident plane, and the *yz* plane as the output plane, there are crossed polarizations in the output plane, akin to those happen in anisotropic structures. The off-diagonal elements in the matrix of Eq. (**S5**) indicate the coupling between E_x and E_y, which is the geometric-phase origin of the spin-locking effect. Particularly, the dependence of the scattering matrix on the angular coordinate ϕ results in the spin split observed in our experiment. According to our paraxial optical imaging system, we have $\theta \to \pi/2$ and $\phi \to 0$, and Eq. (**S5**) is simplified as

$$\begin{bmatrix} E_{sy} \\ E_{sz} \end{bmatrix} = \frac{e^{\mathrm{i}k(r-z)}}{-\mathrm{i}kr} \begin{bmatrix} -S_1\phi & S_1 \\ -S_2 & -S_2\phi \end{bmatrix} \begin{bmatrix} E_x \\ E_y \end{bmatrix}.$$

Let us define $\alpha_1 = \frac{S_1+S_2}{2}, \alpha_2 = \frac{S_1-S_2}{2}$, then

$$\begin{bmatrix} -S_1\phi & S_1 \\ -S_2 & -S_2\phi \end{bmatrix} = \alpha_1 \begin{bmatrix} -\phi & 1 \\ -1 & -\phi \end{bmatrix} + \alpha_2 \begin{bmatrix} -\phi & 1 \\ 1 & \phi \end{bmatrix}. \quad \text{(S6)}$$

Eq. (**S6**) describes a universal geometric phase effect in scattering from α_2. While α_1 and α_2 are determined by the size and refractive index of the particle, the geometric phase spatial profile is determined only by the incident wave and observation direction, regardless of the properties of the nanoparticle.

E. Theoretical results from our model

The theoretical model has been described in the Methods section of the main text, and its schematic illustration is also shown in Fig.S10, using gold nanoparticles with a diameter of 200 nm as an example. Compared to the main text Fig. 2, we show more details in the second scattering, particularly, the second scattering is also

highly directional. This directionality is a key feature in the complex scattering system and it contributes to our observed macroscale effects. In our theoretical model, all directional effects have been considered during the two-step scattering process, and we show that the theoretical results agree well with the experiments (Fig. S11 and Fig. S12).

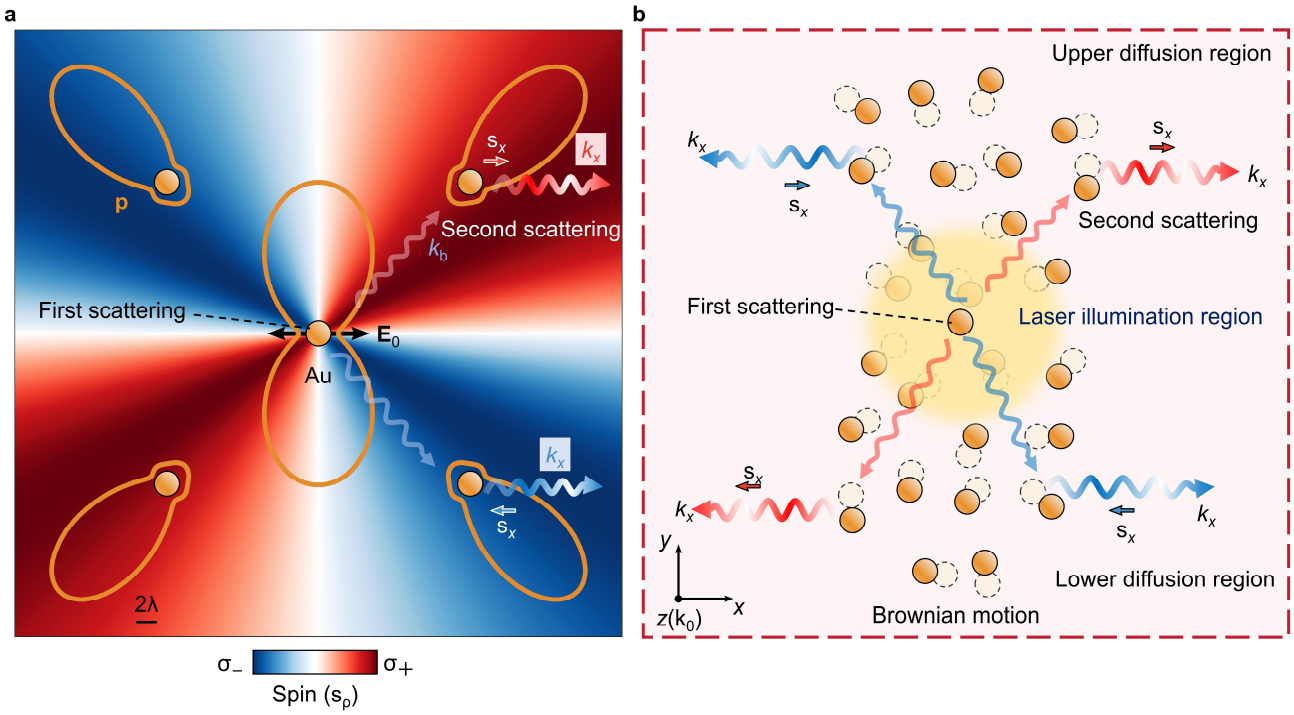

Fig.S10 Schematic illustration of the first and second scattering processes. (**a**) An AuNP is excited by *x*-polarized incident light $\mathbf{E}_0$, leading to the first scattering. The four surrounding nanoparticles are subsequently illuminated by oppositely polarized scattered light and undergo second scattering. The orange curves represent the kinetic momentum density **p** for each scattering. (**b**) Particles in upper diffusion region and lower diffusion region are excited by oppositely polarized scattered light. The reddish arrow stands for right-circular polarization, while the bluish arrow stands for left-circular polarization.

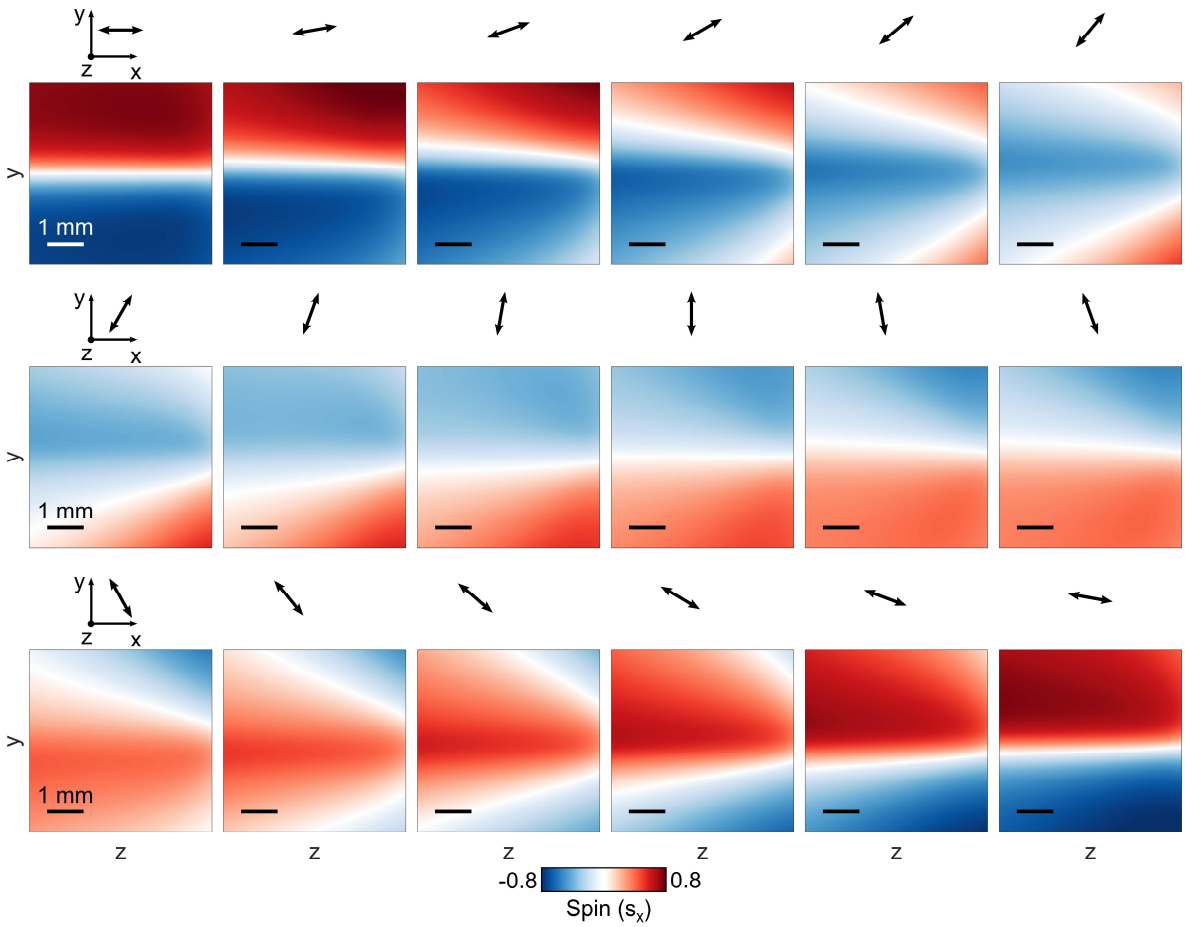

Fig.S11 Theoretical results under different linear polarizations. The black arrows on the top of each image represent the polarization of incident light in the *xy* plane. The images are captured in the *yz* plane, for the samples of AuNPs <*D*> = 200 nm. The results agree with the experimental results in Fig. S4.

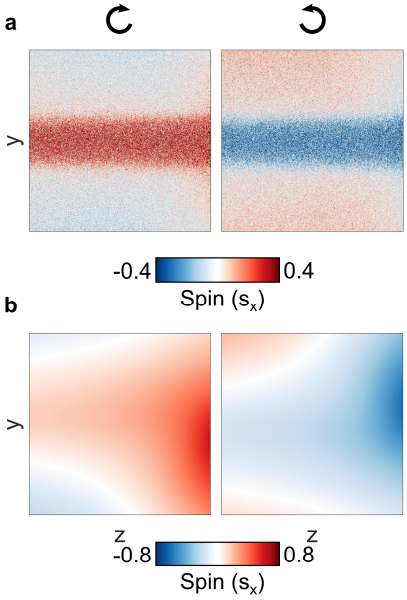

Fig.S12 Experimental and theoretical results under circular polarizations. From left to right, left-handed circular polarization and right-handed circular polarization. The images are captured in the *yz* plane, for the samples of AuNPs <*D*> = 200 nm.

Section S9. SAM density distribution of a focused beam

We give a comparison between our BSLE and the transverse spin from focused beams by introducing the theory of the latter (*16*). The electric and magnetic fields of a focused are

$$\mathbf{E} = \frac{\hat{\boldsymbol{e}}_x + m\hat{\boldsymbol{e}}_y - \frac{x+my}{q(z)}\hat{\boldsymbol{e}}_z}{\sqrt{1+|m|^2}} A(\rho, z)\exp(\mathrm{i}kz),$$
$$\mathbf{H} = \frac{k}{\omega\mu}\frac{\hat{\boldsymbol{e}}_y - m\hat{\boldsymbol{e}}_x - \frac{y-mx}{q(z)}\hat{\boldsymbol{e}}_z}{\sqrt{1+|m|^2}} A(\rho, z)\exp(\mathrm{i}kz).$$

Here, $A(\rho,z) = A_0 \frac{z_R}{q(z)} \exp\left[\mathrm{i}k\frac{\rho^2}{2q(z)}\right], q(z) = z - \mathrm{i}z_R,\ z_R = k\omega_0^2/2\,, \rho = \sqrt{x^2+y^2}$.

The SAM density is given by

$$\mathbf{s} = \mathrm{Im}\left[\frac{\varepsilon}{4\omega}\mathbf{E}^* \times \mathbf{E} + \frac{\mu}{4\omega}\mathbf{H}^* \times \mathbf{H}\right] = \frac{\varepsilon}{2\omega}|A(\rho,z)|^2\left[\sigma\hat{\boldsymbol{e}}_z + \frac{1}{|q(z)|^2}(\sigma xz - yz_R)\hat{\boldsymbol{e}}_x + \frac{1}{|q(z)|^2}(\sigma yz + xz_R)\hat{\boldsymbol{e}}_y\right].$$

Here, $\tau = \frac{1-|m|^2}{1+|m|^2}, \chi = \frac{2\mathrm{Re}m}{1+|m|^2}, \sigma = \frac{2\mathrm{Im}m}{1+|m|^2}$ are Stokes parameters.

Considering that the incident light is linearly polarized, namely, $\sigma = 0$, the SAM density is

$$\mathbf{s} = \frac{\varepsilon}{2\omega}\frac{|A(\rho,z)|^2 z_R}{|q(z)|^2}\left[-y\hat{\boldsymbol{e}}_x + x\hat{\boldsymbol{e}}_y\right].$$

The SAM density is a chiral texture in the *xy* plane, locked with the incident $\boldsymbol{k}$ following a right-handed rule. Therefore, the spin distribution is independent of the polarization direction of the focused beam (Fig. S13), which is different from our experimental results shown in main text Fig. 4 and Fig. S4.

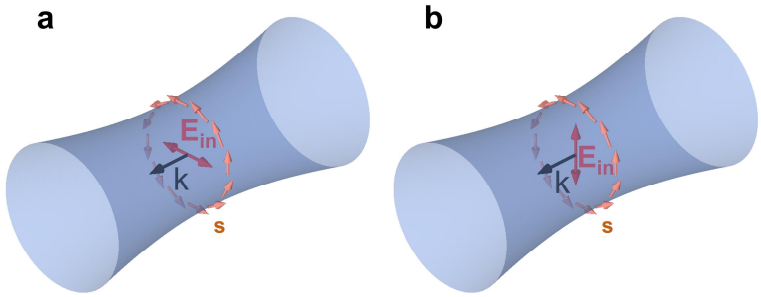

Fig. S13 SAM density distribution of a focused beam. The SAM (orange) is produced by the linearly polarized light along the *x* direction **(a)** and *y* direction **(b)**, respectively. Here the black arrow indicates the direction of the wave vector **k**.

Section S10. The spin from different particle diameters

Figure S14 shows the calculated Mie scattering coefficients $|a_n|$, $|b_n|$ and their phases with the diameter of an AuNP sphere from 20-600 nm (incident wavelength 639 nm, *x*-polarized illumination). When the diameter is smaller than 50 nm, $|a_2|$, $|a_3|$, $|a_4|$, $|b_1|, |b_2|$, $|b_3|, |b_4| \ll |a_1|$ and the spin density is perpendicular to the $\hat{\boldsymbol{e}}_{\boldsymbol{r}}$, $s \propto 1/r^3$. In this region, the scattering is dominated by electric dipole. When the diameter is between 50 and 250 nm, both electric quadrupole and magnetic dipole arise (Fig. S14a), with non-0 and non-π phases between each other (Fig. S14b). According to Eq. (**S5**), the spin-locking effect is in agreement with the experimental observations. As the size of nanoparticle increases, the spin pattern in the *yz* plane becomes more complicated (Fig. S14c) , but the *xy* plane always remains a four-lobe spin distribution, as predicted by Eq. (**S6**).

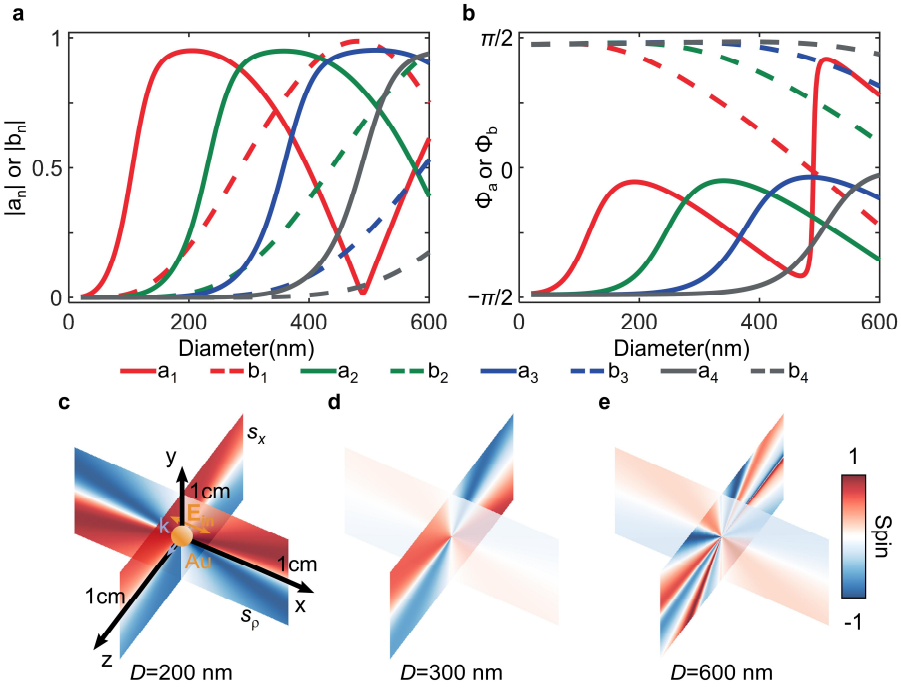

Fig. S14 Mie coefficients, their phases, and SAM density distribution for AuNP of different sizes. (a) Calculated Mie coefficients, **(b)** their phases for a single AuNP as a function of diameter. Solid and dotted lines indicate electric and magnetic components respectively. SAM density distribution in the *xy* plane and *yz* plane of a 200 nm-sized AuNP **(c)**, 300 nm-sized AuNP **(d)**, and 600 nm-sized AuNP **(e)**.

Section S11. Dynamic Light Scattering (DLS) theory

In parallel with our BSLE, we used a dynamic light scattering device (Litesizer 500 from Anton Paar) and scanning electron microscope (SEM, Zeiss Ultra Plus Field Emission Scanning Electron Microscope) to characterize the particle size of our samples and to compare these results with our optical spin-resolved method.

DLS is based on the Brownian motion of scattering particles in a suspension or a liquid solution. When a single wavelength laser illuminates the particles, the laser is scattered to all directions. The scattering intensity changes with time due to the random movement of the particles. Particularly, smaller particles diffuse faster, causing more rapid fluctuations in the intensity. This random fluctuation of light intensity can be used to extract a diffusion coefficient and calculate the particle size.

The intensity temporal autocorrelation function $g^2(\tau) = \langle I(t) \times I(t+\tau)\rangle / \langle I^2(t)\rangle$ is related to the electric field correlation function $g^1(\tau)$ by the Siegert relation $g^2(\tau) = 1 + \beta|g^1(\tau)|^2$ (*17*), where β is a factor related to the geometry and collimation of the laser, $I(t)$ is the intensity of light, and τ is the time lag value.

The coherence time τ_c of the scattered light can be derived from $g^1(\tau) = \exp(-\Gamma\tau) = \exp(-\tau/\tau_c)$, with $\Gamma = D_t q^2$ and $q = (4\pi n/\lambda) sin(\theta/2)$ is the wave vector. $\lambda =$ 658 nm is the wavelength of the incident laser; n is the refractive index of the sample; θ is the angle between the detector and the sample. Hydrodynamic radius was calculated according to the autocorrelation analysis of scattered light intensity data based on translation diffusion coefficient by the Stokes-Einstein relation (*18*):

$$D_h = k_B T/3\pi\eta D_t,$$

where D_h, D_t, k_B, $T = 298\,K$ and $\eta = 0.89\,mP_a$ are the hydrodynamic diameter, translational diffusion coefficient, Boltzmann's constant, thermodynamic temperature, and viscosity of the water, respectively.

The AuNPs and Fe_3O_4 particles were hosted in 1-cm-optical-path quartz cuvettes after being diluted. The particle size distribution and mean diameter were measured by a DLS device with three fixed scattering angles of 15°, 90° and 175° respectively, at 25°C. The results for AuNPs and Fe_3O_4 are shown in Fig. S15 and Fig. S16, respectively. Meanwhile, AuNPs and Fe_3O_4 particles were also characterized using SEM (Fig. S15 and Fig. S16), to compare with the results from DLS measurements and our optical spin-resolved spectroscopy.

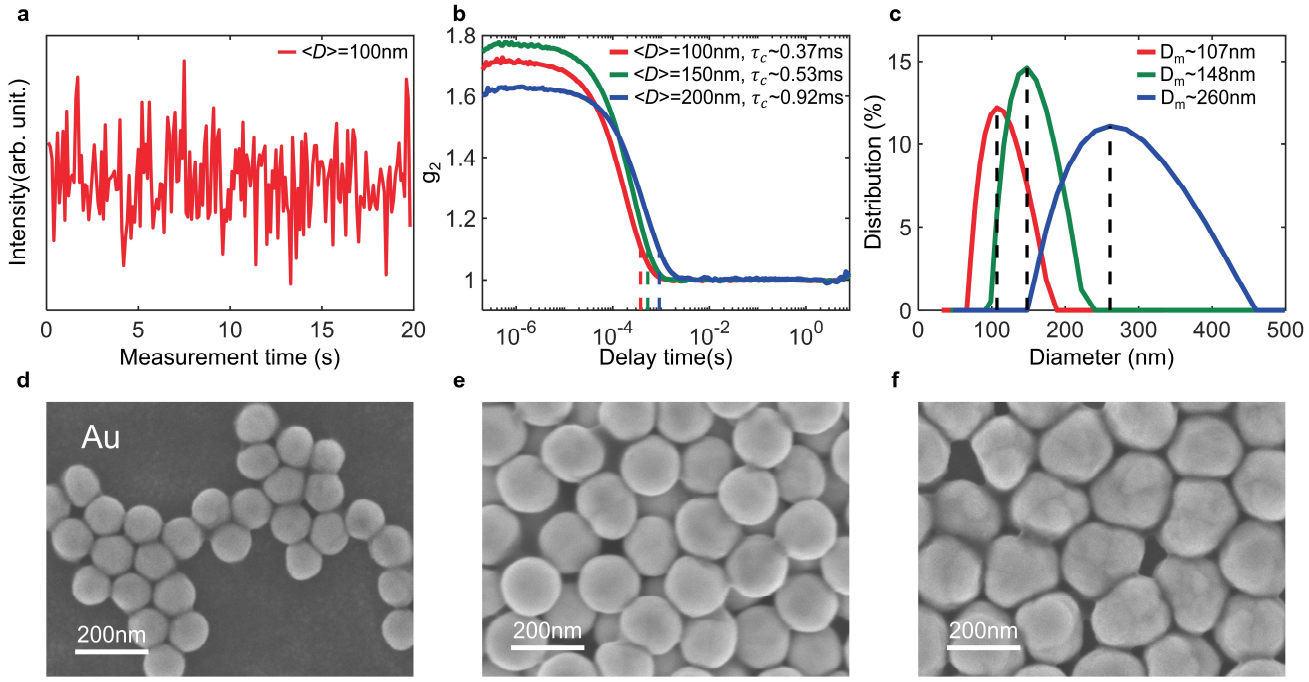

Fig. S15 **(a)** Measured $I(t)$ by a DLS device, **(b)** autocorrelation function $g^2(\tau)$ and **(c)** size distributions of AuNPs. **(d-f)** SEM images of AuNPs corresponding to mean diameters of 100, 150 nm and 200 nm, from

left to right, respectively.

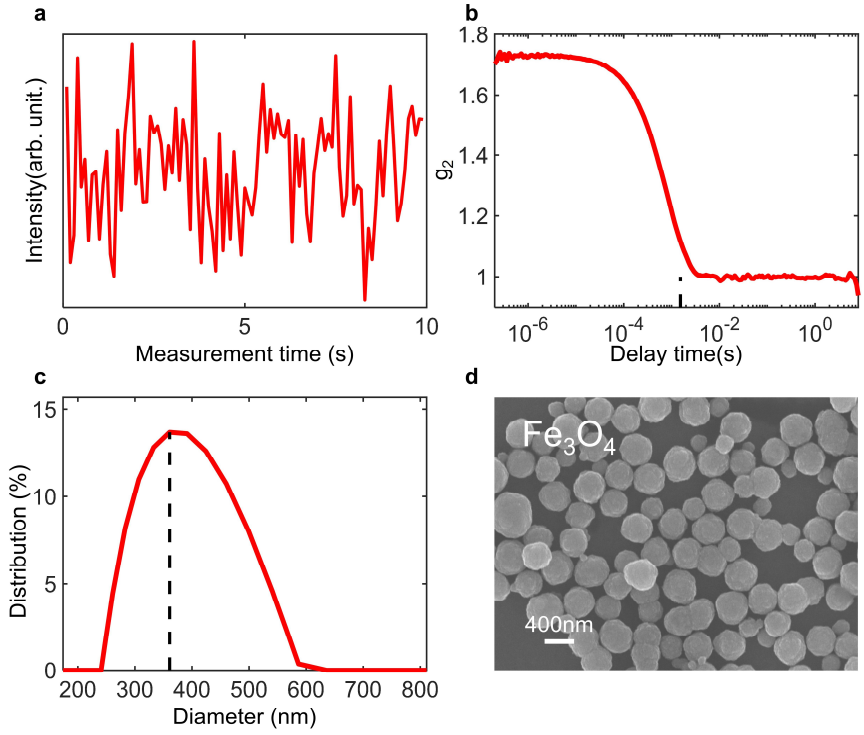

Fig. S16 (**a**) Measured $I(t)$ by a DLS device, (**b**) autocorrelation function $g^2(\tau)$ and (**c**) size distribution of monodisperse Fe_3O_4 particles. (**d**) SEM image of Fe_3O_4 particles with mean diameter of 360.8 nm.

Section S12. Evaluate the experimentally obtained spin-resolved spectra

We give detailed calculation method for obtaining the results in main text Fig. 5. We randomly placed N_p = 10^4 particles in a region of 2 mm × 2 mm × 2 cm, with all the particles the same size, D. We defined an observation region centered at x = 0 mm, y = 2.7 mm and z = 5 mm with a perturbation region of 1.2 mm × 1.2 mm in the yz plane. This region is set to simulate the size of the pinhole. Then, we randomly select N_m = 300 observation points within this region and calculate the left-handed circularly polarized light intensity with $\bar{I}_L(\lambda) = 0.5\,\mathrm{abs}\left(E_y + \mathrm{i}E_z\right)^2$ and the right-handed circularly polarized light intensity with $\bar{I}_R(\lambda) = 0.5\,\mathrm{abs}\left(E_y - \mathrm{i}E_z\right)^2$. After averaging the intensities over the 300 observation points to obtain the average intensity distributions $\bar{I}_L(\lambda)$ and $\bar{I}_R(\lambda)$, we calculated the spin distribution $s_x(\lambda) = \left(\bar{I}_R(\lambda) - \bar{I}_L(\lambda)\right)/\left(\bar{I}_R(\lambda) + \bar{I}_L(\lambda)\right)$. We set the particle diameters' range from 50 nm to 450 nm, with a 5 nm interval, to obtain a series of spin density spectral curves, as shown in Fig. 5d. Note that the numbers of N_p and N_m are chosen to balance calculation time and stability. Similar results can be observed with different numbers.

To validate the effectiveness of our numerical simulation, we calculated the root mean square error (RMSE) between the experimental spin spectrum and a series of theoretical curves. The difference between the theoretical and experimental results arises from the varying concentrations of nanoparticles, which is a depolarization process making the value of the theory spin different from our observed spin. To take this process into consideration, we introduce a depolarization parameter $dpol$ (from 0 to 1) to calibrate the spin between the experiment and the simulation. Therefore, once we have obtained an experimental spin spectrum, we can use particle size *D* and the depolarization parameter *dpol* to compare the theoretical and experimental results. The agreement between the theoretical and experimental spin spectra is characterized by $\mathrm{RMSE} = \sqrt{\frac{1}{n}\sum_{i=1}^{n}\left(x_i^{exp} - x_i^{theo}\right)^2}$, where $x_i^{exp} = s_x^{exp}(\lambda_i)$, $x_i^{theo} = dpol \times s_x^{theo}(\lambda_i)$, $dpol$ is related to the concentration and n represents the number of wavelength points in experimental spin spectrum. After substituting these parameters, we have

$$\mathrm{RMSE} = \sqrt{\frac{1}{n}\sum_{i=1}^{n}\left(s_x^{exp}(\lambda_i) - dpol \times s_x^{theo}(\lambda_i)\right)^2}.$$

A smaller RMSE indicates a better agreement between the theoretical and experimental results. The change of RMSE with respect to $dpol$ and the theoretical diameter of the nanoparticle is shown in Fig. S17. The Correlation is equal to 1 – RMSE as shown in Fig. 5b. For AuNPs with the particle diameter of <*D*> = 100 nm used in the experiment, the best theoretical corresponding diameter of nanoparticle is 100 nm. At this point, $dpol = 1$, $\mathrm{RMSE} \approx 0.022$. For AuNPs with the particle diameter of <*D*> = 150 nm used in the experiment, the best theoretical corresponding diameter of nanoparticle is 135 nm. At this point, $dpol = 0.79$, $\mathrm{RMSE} \approx 0.032$. For AuNPs with the particle diameter of <*D*> = 200 nm used in the experiment, the best theoretical corresponding diameter of nanoparticle is 195 nm. At this point, $dpol = 0.23$, $\mathrm{RMSE} \approx 0.032$.

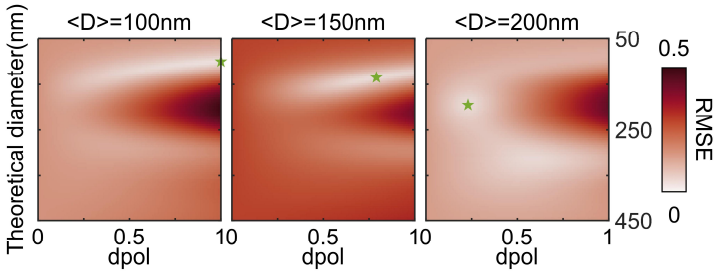

Fig. S17 RMSE distribution with respect to $dpol$ and theoretical diameter of the nanoparticle. The value of RMSE is minimal at the location marked by the green star. The corresponding $dpol$ and theoretical diameter are used to calculate Fig. 5d.

Section S13. Statistics of the scattering from incoherent to coherent regions

As mentioned in the main text, we establish a two-part scattering theory to evaluate the complex scattering of light in this Brownian system. (i) A two-step scattering process for each combination of two particles: one in the illumination region and another in the diffusion region. The light field of the incident laser, $\mathbf{E}_0$, excites one of the nanoparticles in the illumination region $\mathbf{r}_b$, resulting in a radiation source, $\mathbf{E}_b = \mathbf{M}\times\mathbf{E}_0$. Here, $\mathbf{M}$ is the Mie scattering operator. In addition, another particle in the diffusion region $\mathbf{r}_d$ is similarly excited by $\mathbf{E}_b$, resulting in $\mathbf{E}_d = \mathbf{M}\times\mathbf{E}_b$. For a simplified analysis, the second scattering can be considered approximately $\mathbf{E}_d \propto \mathbf{E}_b(\mathbf{r}')$, with $\mathbf{r}' = \mathbf{r}_d\text{-}\mathbf{r}_b$. (ii) The field is a superposition of $\mathbf{E}_d$ from many particles with different $\mathbf{r}_b$. This process is sketched in Fig. S18.

For incoherent scattering, we first project the field $\mathbf{E}_b(\mathbf{r}')$ onto the spin-up and spin-down states, obtaining the opposite spin intensities $I_R(\mathbf{r}')$ and $I_L(\mathbf{r}')$, respectively. The intensities are summed over all particles, and $I_{R,L}(\mathbf{r_d}) = \sum_{\mathbf{r_b}} I_{R,L}(\mathbf{r}_d - \mathbf{r}_b)$. For the coherent case, we directly sum all field $\mathbf{E}_b(\mathbf{r}')$ from illumination particles to obtain the electric field $\mathbf{E}(\mathbf{r}_d) = \sum_{\mathbf{r}_b} \mathbf{E}_b(\mathbf{r}_d - \mathbf{r}_b)$, and then projecting this field onto spin-up and spin-down states to have the opposite spin intensities $I_R(\mathbf{r}_d)$ and $I_L(\mathbf{r}_d)$. In general, the scattering theory can be developed to partial coherence (*19*). Here, we statistically divide the system composed of N nanoparticles into m equal parts. Within each part, the scattering from these particles is coherent, but between different parts, the fields are completely incoherent. This simple approach provides us an artificial parameter characterized by $m/N\in[0,1]$, through which we can describe a clear evolution of the scattering property from incoherent to coherent. The scattering within the same group is coherent, and the electric field is superposed as: $\mathbf{E}_m = \sum_n \mathbf{E}_{mn}$. Scattering between different groups is incoherent, and the light intensity is superposed as: $I_R = 0.5\sum_m \mathrm{abs}(E_{my} - \mathrm{i}E_{mz})^2$, $I_L = 0.5\sum_m \mathrm{abs}(E_{my} + \mathrm{i}E_{mz})^2$. The spin is then calculated as $s_x = (I_R - I_L)/(I_R + I_L)$. This process is repeated 10^4 times to minimize statistical error. By changing m/N from 100% to 0.01%, the corresponding curves, shown in Fig. S19d from left to right, which indicate that the most significant spin split phenomenon occurs in the incoherent scenario. The reduction of m/N will diminish this effect until the phenomenon disappears in a coherent disordered system. As m/N decreases, the absolute

value of the skewness in Fig. S19d (spin panel) is about 0.056 for $m/N = 100\%$, 0.433 for $m/N = 0.08\%$, 0.639 for $m/N = 0.02\%$, 0.610 for $m/N = 0.01\%$. The skewness of reddish curve is positive, while that of the bluish curve is negative.

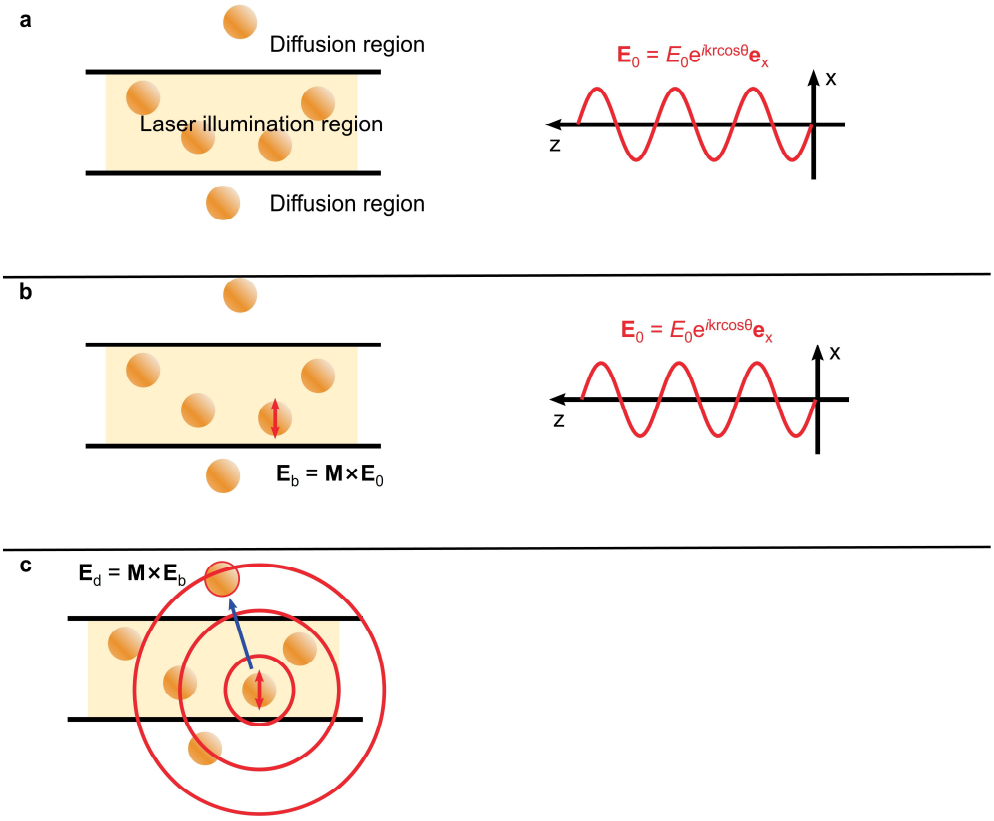

Fig. S18 Sketched essential scattering processes. (a) Schematic of scattering system. **(b)** First step: The incident laser field, $\mathbf{E}_0$, excites one of the nanoparticles in the illumination region, resulting in a radiation source $\mathbf{E}_b = \mathbf{M}\times\mathbf{E}_0$. Here, $\mathbf{M}$ represents the Mie scattering matrix**. (c)** Second step: Another nanoparticle in the diffusion region is similarly excited by $\mathbf{E}_b$, resulting in $\mathbf{E}_d = \mathbf{M}\times\mathbf{E}_b$.

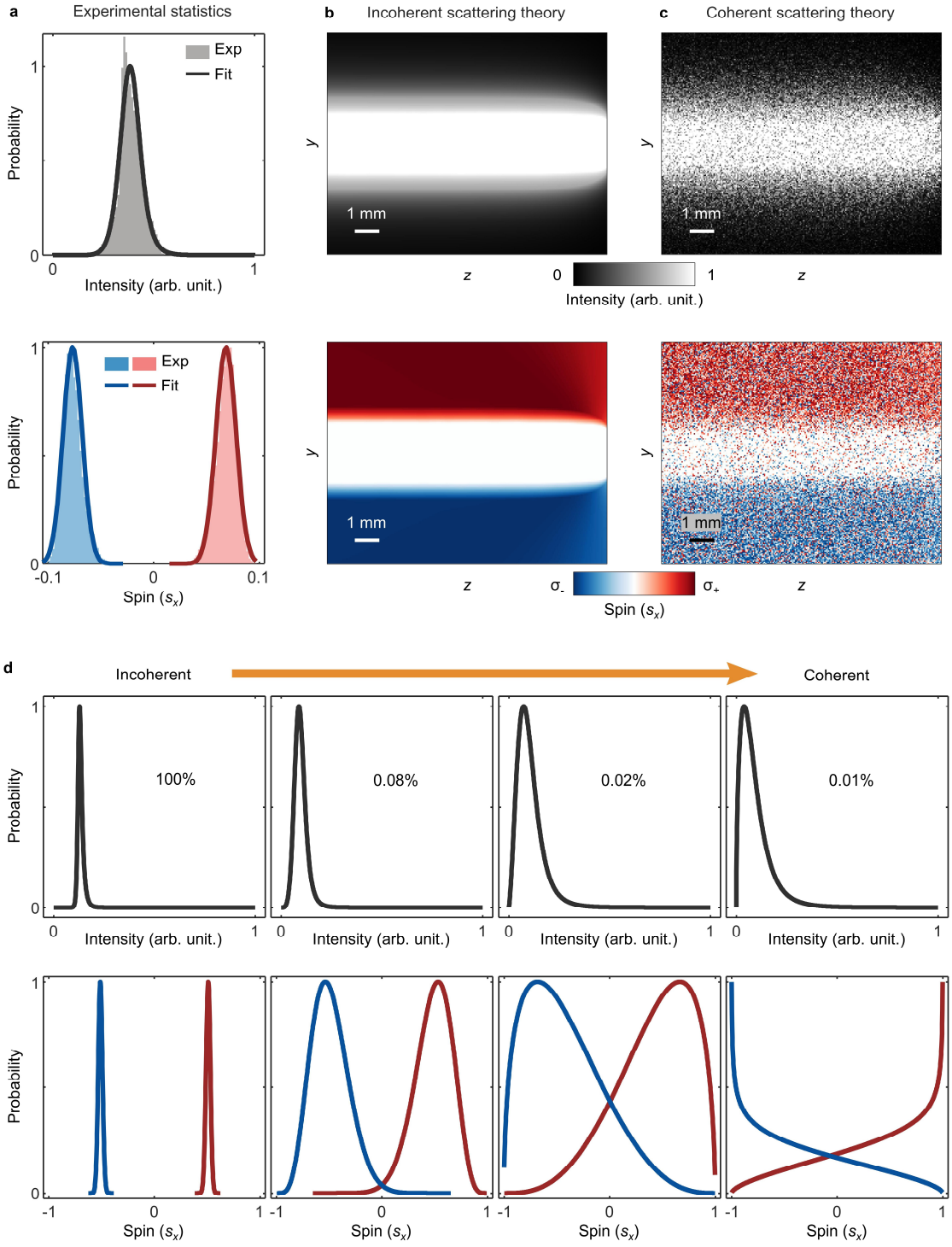

Fig. S19. Statistical properties of the BSLE and incoherent scattering theory. (**a**) The histograms are experimentally observed statistical distributions of the spatial intensity (upper panel) and spin (lower panel), which are obtained from the diffusion regions of Fig. 1d and 1e, respectively. The solid curves are fitted using a Burr distribution for the intensity and a Beta distribution for the spin. (**b**) The calculated spatial distributions of the normalized intensity and spin from the incoherent scattering theory. (**c**) The calculated spatial distributions of the normalized intensity and spin from the coherent scattering theory. (**d**) The theoretical evolution of the intensity and spin distributions by changing *m*/*N* from 100% (incoherent) to 0.01% (coherent). As the degree of coherence increases, the spin distributions become wider with enhanced skewness, corresponding to increased spin fluctuations that reduce the spin-locking phenomenon.

Supplementary References

1. M. Xu, R. Alfano, Circular polarization memory of light. *Physical Review E—Statistical, Nonlinear, and Soft Matter Physics* **72**, 065601 (2005).
2. M. Xu, R. R. Alfano, Random walk of polarized light in turbid media. *Physical review letters* **95**, 213901 (2005).
3. C. F. Bohren, D. R. Huffman, *Absorption and scattering of light by small particles*. (John Wiley & Sons, 2008).
4. P. Shi, L. Du, C. Li, A. V. Zayats, X. Yuan, Transverse spin dynamics in structured electromagnetic guided waves. *Proceedings of the National Academy of Sciences* **118**, e2018816118 (2021).
5. A. J. Vernon, S. Golat, C. Rigouzzo, E. A. Lim, F. J. Rodríguez-Fortuño, A decomposition of light's spin angular momentum density. *Light: Science & Applications* **13**, (2024).
6. K. Y. Bliokh *et al.*, Spin-to-orbital angular momentum conversion in focusing, scattering, and imaging systems. *Optics express* **19**, 26132-26149 (2011).
7. M. Chen, M. Kim, A. M. Wong, G. V. Eleftheriades, Huygens' metasurfaces from microwaves to optics: a review. *Nanophotonics* **7**, 1207-1231 (2018).
8. M. Kerker, D.-S. Wang, C. Giles, Electromagnetic scattering by magnetic spheres. *JOSA* **73**, 765-767 (1983).
9. M. F. Picardi, A. V. Zayats, F. J. Rodríguez-Fortuño, Janus and Huygens dipoles: near-field directionality beyond spin-momentum locking. *Physical review letters* **120**, 117402 (2018).
10. Y. Cheng *et al.*, Directional dipole dice enabled by anisotropic chirality. *Proceedings of the National Academy of Sciences* **120**, e2301620120 (2023).
11. X. Zambrana-Puyalto, I. Fernandez-Corbaton, M. Juan, X. Vidal, G. Molina-Terriza, Duality symmetry and Kerker conditions. *Optics letters* **38**, 1857-1859 (2013).
12. K. Chen *et al.*, Directional janus metasurface. *Advanced Materials* **32**, 1906352 (2020).
13. M. F. Picardi *et al.*, Experimental demonstration of linear and spinning Janus dipoles for polarisation-and wavelength-selective near-field coupling. *Light: Science & Applications* **8**, 52 (2019).
14. B. Wang *et al.*, Visible-frequency dielectric metasurfaces for multiwavelength achromatic and highly dispersive holograms. *Nano letters* **16**, 5235-5240 (2016).
15. K. Y. Bliokh, A. Niv, V. Kleiner, E. Hasman, Geometrodynamics of spinning light. *Nature Photonics* **2**, 748-753 (2008).
16. K. Y. Bliokh, F. Nori, Transverse and longitudinal angular momenta of light. *Physics Reports* **592**, 1-38 (2015).
17. R. J. Glauber, The quantum theory of optical coherence. *Physical Review* **130**, 2529 (1963).
18. A. Einstein, Über die von der molekularkinetischen Theorie der Wärme geforderte Bewegung von in ruhenden Flüssigkeiten suspendierten Teilchen. *Annalen der physik* **4**, (1905).
19. J. W. Goodman, *Statistical optics*. (John Wiley & Sons, 2015).
20. C. Forbes, M. Evans, N. Hastings, B. Peacock, *Statistical distributions*. (John Wiley & Sons, 2011).
21. C. Kleiber, *Statistical Size Distributions in Economics and Actuarial Sciences*. (John Wiley &Sons, Inc, 2003).